ADVANCED MATERIALS

www.advmat.de

Kinetic Stabilization of the Sol–Gel State in Perovskites Enables Facile Processing of High-Efficiency Solar Cells

Kai Wang, Ming-Chun Tang, Hoang X. Dang, Rahim Munir, Dounya Barrit, Michele De Bastiani, Erkan Aydin, Detlef-M. Smilgies, Stefaan De Wolf, and Aram Amassian**

Perovskite solar cells increasingly feature mixed-halide mixed-cation compounds ($FA_{1-x-y}MA_xCs_yPbI_{3-z}Br_z$) as photovoltaic absorbers, as they enable easier processing and improved stability. Here, the underlying reasons for ease of processing are revealed. It is found that halide and cation engineering leads to a systematic widening of the anti-solvent processing window for the fabrication of high-quality films and efficient solar cells. This window widens from seconds, in the case of single cation/halide systems (e.g., $MAPbI_3$, $FAPbI_3$, and $FAPbBr_3$), to several minutes for mixed systems. In situ X-ray diffraction studies reveal that the processing window is closely related to the crystallization of the disordered sol–gel and to the number of crystalline byproducts; the processing window therefore depends directly on the precise cation/halide composition. Moreover, anti-solvent dripping is shown to promote the desired perovskite phase with careful formulation. The processing window of perovskite solar cells, as defined by the latest time the anti-solvent drip yields efficient solar cells, broadened with the increasing complexity of cation/halide content. This behavior is ascribed to kinetic stabilization of sol–gel state through cation/halide engineering. This provides guidelines for designing new formulations, aimed at formation of the perovskite phase, ultimately resulting in high-efficiency perovskite solar cells produced with ease and with high reproducibility.

With record power conversion efficiencies (PCE) close to 24%, perovskite solar cells (PSCs) hold great promise to combine high photovoltaic performance with low processing cost.[1–4] This combination can be ascribed to several factors, such as the remarkable optoelectronic properties of perovskites–evidenced by a sharp absorption onset, a small Urbach energy, and a low exciton binding energy–as well as the fact that perovskites use earth-abundant elements.[5–7] The organic–inorganic metal halide perovskites used in such devices feature the characteristic AMX_3 structure, where A is an organic or inorganic cation, most often methylammonium ($CH_3NH_3^+$, MA^+), formamidinium ($HC(NH_2)_2^+$, FA^+), or cesium (Cs^+), M is a metal cation, such as Pb^{2+} or Sn^{2+}, and X is a monovalent anion (halide ion Cl, Br, or I).[8–10]

Various deposition techniques have been developed to obtain polycrystalline perovskite films, including spin-, dip-, and blade-coating, as well as vacuum-based processes.[11,12] To date, one-step spin coating remains the most popular and facile implementation to fabricate high-quality hybrid perovskite thin films from solution. The device efficiency and stability are strongly dictated by the electronic properties and trap state densities in the perovskite film. These, in turn, are influenced by the film crystallization, its morphology, and the presence of defects and imperfections.[13,14] However, despite the simplicity of the one-step deposition, the exact mechanisms underlying the growth process, from precursor solution to solid-state film, and the crystallization mechanism within the sol–gel state, are still poorly understood. This lack of information is partially caused by the heavy reliance on post-deposition ex situ characterization methods to date.[15,16] Recently, in situ time-resolved grazing-incidence wide-angle X-ray scattering (GIWAXS) has emerged as a powerful technique to study the microstructural evolution from the solution-precursor to the solid state, revealing the crystallization behavior and formation of crystalline intermediates and byproducts.[17,18] Using in situ GIWAXS methods, the classic $MAPbI_3$ perovskite material has already been investigated; Gong and coworkers identified the

Dr. K. Wang, M.-C. Tang, Dr. H. X. Dang, Dr. R. Munir,[+]
D. Barrit, Dr. M. De Bastiani, Dr. E. Aydin, Prof. S. De Wolf,
Prof. A. Amassian
King Abdullah University of Science and Technology (KAUST)
Division of Physical Science and Engineering, and KAUST Solar Center
Thuwal 23955-6900, Saudi Arabia
E-mail: stefaan.dewolf@kaust.edu.sa; aamassi@ncsu.edu

Dr. H. X. Dang, Prof. A. Amassian
Department of Materials Science and Engineering
North Carolina State University
Raleigh, NC 27695, USA

Dr. D.-M. Smilgies
Cornell High Energy Synchrotron Source (CHESS)
Cornell University
Ithaca, NY 14850, USA

The ORCID identification number(s) for the author(s) of this article can be found under https://doi.org/10.1002/adma.201808357.

[+]Present address: Helmholtz-Zentrum Berlin für Materialien und Energie GmbH, Berlin 12489, Germany

DOI: 10.1002/adma.201808357

© 2019 WILEY-VCH Verlag GmbH & Co. KGaA, Weinheim

existence of an intermediate phase during its crystallization process,[19] whereas Chen and coworkers found that the coexistence of *N*,*N*-dimethylformamide (DMF) and dimethyl sulfoxide (DMSO) leads to a longer crystallization time and more nucleation sites. With these insights the DMSO concentration was then fine-tuned to improve solar cell performance.[20] Our group reported the solution-to-solid conversion during spin-coating of $MAPbX_3$ (X = I, Br, and Cl) in DMF by in situ GIWAXS and disclosed the various solidification pathways for different halide compositions.[21] The role of various anti-solvent drip strategies has also been unraveled by in situ GIWAXS in the case of $MAPbI_3$,[22,23] whereas other studies have shed light on the formation of reduced-dimensional perovskites.[24–26] In recent years, mixed-cation mixed-halide perovskites have emerged for their superior ease of processing, reproducibility, and device performance, compared to $MAPbI_3$ and $FAPbI_3$.[27,28] However, the precise solution-to-solid conversion of these advanced formulations is yet to be revealed, and their improved processability in the context of anti-solvent dripping is yet to be quantified, let alone understood. Such knowledge potentially holds important clues to further progress in formulation engineering.[29–33] To accurately describe the intermediate phases during spin-coating, we adopt the Ramsdell notation, employed by Gratia et al.[34] For example, the well-known yellow δ phase, called here the 2H phase, is a nonperovskite phase composed of pure hexagonal closed-packed AX_3 layers, resulting in a 1D array of BX_6 face-sharing octahedra. The photoactive α phase, which is the desired perovskite phase, called here the 3C phase, is composed of cubic closed-packed AX_3 layers, resulting in a 3D framework of BX_6 corner-sharing octahedral. The other intermediate 4H phase, which is again a nonperovskite phase, is composed of a combination of a hexagonal and cubic closed-packed AX_3 stacking sequence, resulting in a 3D framework of both face-sharing and corner-sharing BX_6 octahedra.

Here, we systematically investigate the roles of cation (FA^+, MA^+, Cs^+, and Rb^+) and halide (I and Br) mixing in FA-dominated perovskite formulations. We do this by building up the compositional complexity of our films toward state-of-the-art mixed cation/mixed halide perovskites $FA_{0.81}MA_{0.14}Cs_{0.05}PbI_{2.55}Br_{0.45}$. Anti-solvent dripping during spin coating–often using chlorobenzene (CB)–has been widely applied to achieve high-quality polycrystalline perovskite films with excellent surface coverage. The drip time for mixed-halide mixed-cation systems has typically been ≈20 s in many studies. We reveal the dynamic microstructural evolution through in situ diagnostics of the precursors solution solidification during spin coating. By this, we unveil the dramatic impact that specific mixtures of cations and halides can have on this solidification process and the subsequent direct conversion to the desirable 3C phase upon anti-solvent drip, enabling facile processing. Systematically we find that for a given perovskite formulation a corresponding anti-solvent dripping time-window exists for producing high-quality films. This window is delineated by the spontaneous collapse of the glassy sol–gel state into crystalline byproducts, which leads to isolated domains, poor morphology, and pinholes. For instance, we find that replacing MA^+ with FA^+ doubles the anti-solvent dripping time window from ≈30 s ($MAPbI_3$) to ≈60 s ($FAPbI_3$), as the latter forms a nonsolvated 2H phase whereas the former incorporates the solvent to form a $MAPbI_3 \cdot DMSO$ co-crystal. Mixing cations and halides hinders further the collapse of the sol–gel precursor by requiring the growth of multiple, compositionally distinct phases. Indeed, formation of segregated phases requires mass transport and segregation of precursor components, such as halides and/or cations, thus extending the lifetime of the sol–gel state. For instance, incorporating a small amount of Br into $FAPbI_3$ further delays the collapse time to ≈90 s by requiring halide segregation to form the 2H phase as well as the 4H phase. Addition of Cs^+ into the mixture promotes formation of three phases: the entropically stabilized 3C perovskite phase, in addition to the 2H and 4H phases. This further delays the sol–gel collapse, now to the 2 min mark. Finally, addition of Rb^+ promotes the formation of a fourth phase, which appears to be solvated, and delays the collapse to 4 min.

Upon anti-solvent dripping, the $FAPbI_3$ formulation converts to the 2H phase instantaneously. The $FA_{0.81}MA_{0.14}Cs_{0.05}PbI_{2.55}Br_{0.45}$ system responds in a more complex but highly desirable way: the 3C perovskite phase and 2H and 4H phases form simultaneously at first, then the latter two convert into the stable 3C perovskite phase. We fabricated large sets of PSCs based on four distinct perovskite compositions ($MAPbI_3$, $FA_{0.81}MA_{0.14}Cs_{0.05}PbI_3$, $FA_{0.81}MA_{0.14}Cs_{0.05}PbI_{2.55}Br_{0.45}$, and $FA_{0.78}MA_{0.12}Cs_{0.05}Rb_{0.05}PbI_{2.55}Br_{0.45}$), exhibiting increasingly long sol–gel lifetimes. Systematically, we fabricated devices within and outside the respective sol–gel stability windows, where we find the device performance fully confirms our observations from in situ GIWAXS. Indeed, we find that highly efficient devices can only be fabricated with anti-solvent dripping within the disordered sol–gel window, which can be tuned by virtue of kinetic stabilization of sol–gel state. Our study reveals new insights into the sol–gel state and its subsequent phase transformation in mixed-halide mixed-cation perovskites, the role of cations and halides, and the importance of their mixture for direct conversion to the desirable perovskite phase.

We begin by investigating the "natural" temporal evolution of microstructure in solution-cast perovskite formulations. For all films, we use the same solvent composition and do not apply any anti-solvent dripping. Initially, we look at the classical $MAPbI_3$, $MAPbBr_3$, $FAPbI_3$, and $FAPbBr_3$ systems. We then extend our study to FA-dominated mixed-cation and mixed-halide (I and Br) precursors solution of increasing complexity to shed light on the effect of specific cations and halides. The studied systems are $FA_{0.86}MA_{0.14}PbI_3$ (denoted as $FAMAPbI_3$), $FA_{0.95}Cs_{0.05}PbI_3$ (denoted as $FACsPbI_3$), $FA_{0.81}MA_{0.14}Cs_{0.05}PbI_3$ (denoted as $FAMACsPbI_3$), $FAPbI_{2.55}Br_{0.45}$, $FA_{0.86}MA_{0.14}PbI_{2.55}Br_{0.45}$ (denoted as $FAMAPbI_{2.55}Br_{0.45}$), $FA_{0.95}Cs_{0.05}PbI_{2.55}Br_{0.45}$ (denoted as $FACsPbI_{2.55}Br_{0.45}$), $FA_{0.81}MA_{0.14}Cs_{0.05}PbI_{2.55}Br_{0.45}$ (denoted as $FAMACsPbI_{2.55}Br_{0.45}$), and $FA_{0.78}MA_{0.12}Cs_{0.05}Rb_{0.05}PbI_{2.55}Br_{0.45}$ (denoted as $FAMACsRbPbI_{2.55}Br_{0.45}$). All perovskite precursors were prepared using a mixture of *N*,*N*-dimethylformamide and dimethyl sulfoxide solvents (4:1 ratio) using the same molarity. All in situ experiments were performed on glass substrates coated with a TiO_2 layer, the same as used in our n–i–p devices.

The in situ 2D GIWAXS snapshots taken at 10, 50, 70, 100, and 150 s are presented in Figure S1 (Supporting Information)

© 2019 WILEY-VCH Verlag GmbH & Co. KGaA, Weinheim

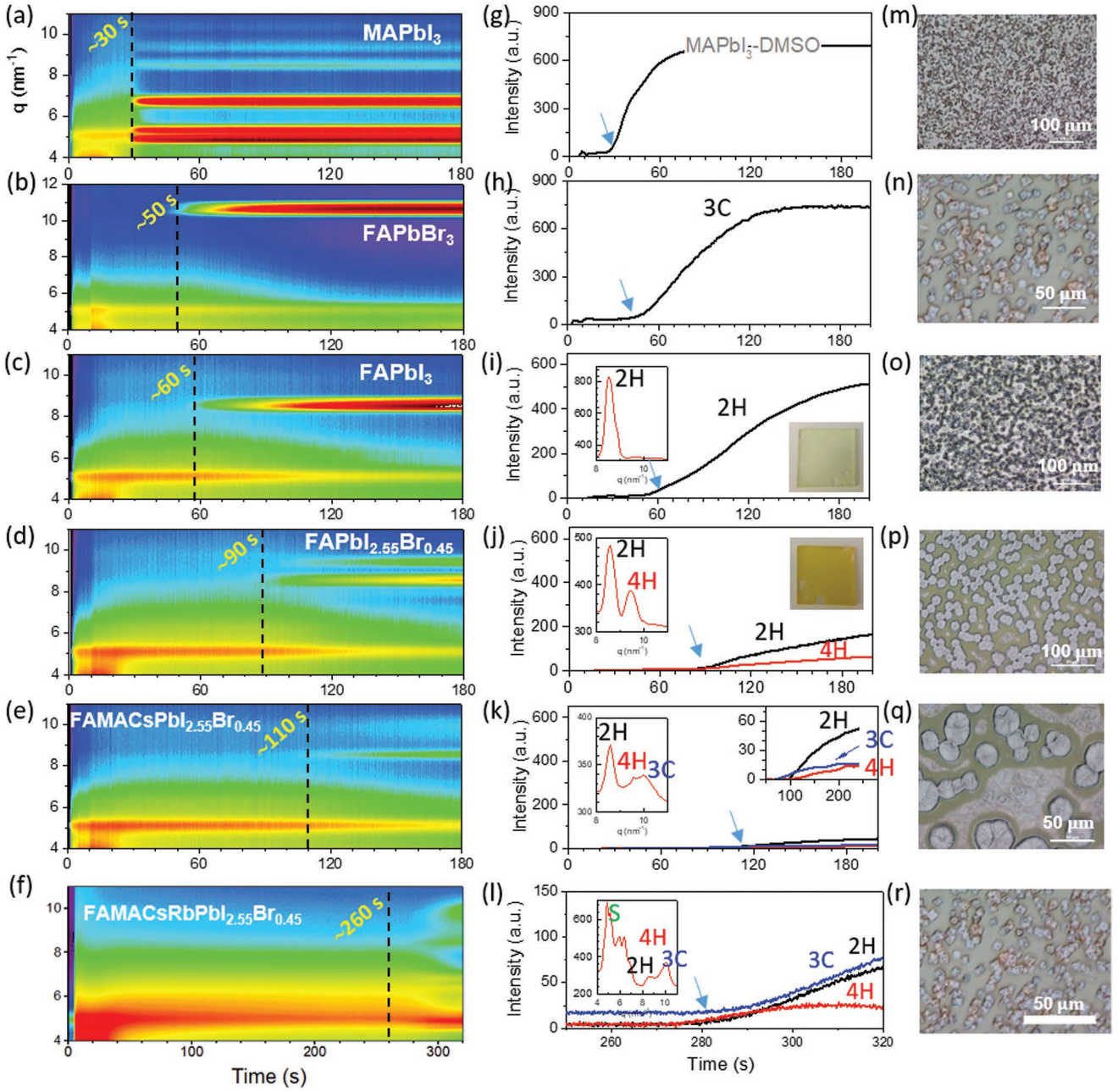

Figure 1. a–f) Time-resolved GIWAXS intensity maps showing the ink-to-solid transformation during spin coating of the following perovskite precursor inks: a) $MAPbI_3$, b) $FAPbBr_3$, c) $FAPbI_3$, d) $FAPbI_{2.55}Br_{0.45}$, e) $FAMACsPbI_{2.55}Br_{0.45}$, and f) $FAMACsRbPbI_{2.55}Br_{0.45}$. g–l) The time evolution of the integrated intensity of the crystalline phases are shown in: g) for the solvate diffraction feature (q = 4.8 nm^{-1}) for $MAPbI_3$, h) the perovskite phase of $FAPbBr_3$, i) the nonperovskite 2H phase (q = 8.5 nm^{-1}) for $FAPbI_3$, j) the 2H and 4H (q = 9.4 nm^{-1}) phases for $FAPbI_{2.55}Br_{0.45}$, k) the 2H, 4H, and 3C phases for $FAMACsPbI_{2.55}Br_{0.45}$ and l) the 2H, 4H, and 3C phases for $FAMACsRbPbI_{2.55}Br_{0.45}$. The insets in (i–l) show the diffraction peak position of the different phases at final spin-coating stage. m–r) Optical microscopy images of the films of $MAPbI_3$, $FAPbBr_3$, $FAPbI_3$, $FAPbI_{2.55}Br_{0.45}$, $FAMACsPbI_{2.55}Br_{0.45}$, and $FAMACsRbPbI_{2.55}Br_{0.45}$.

for a subset of compositions, namely $MAPbI_3$, $FAPbI_3$, $FAPbBr_3$, $FAPbI_{2.55}Br_{0.45}$, and $FAMACsPbI_{2.55}Br_{0.45}$. We summarize in **Figure 1**a–f the typical time-evolution of the scattering features of various perovskite formulations during spin coating. We have done so by integrating the scattering intensity over each time slice of 0.2 s and plotting the 2D scattering intensity maps with respect to time (abscissa; $0 < t < 180$ s) and q (ordinate; $4 < q < 11$ nm^{-1}). The length of the scattering vector q is given by $q = \sqrt{q_z^2 + q_{xy}^2}$, where $q_z = \frac{4\pi \sin \alpha_f}{\lambda}$, $q_{xy} = \frac{4\pi \sin \theta_f}{\lambda}$, and λ is the wavelength of the X-ray beam. In all cases, we observe the presence of a wet, colloidal precursor as indicated by the formation of a broad scattering halo at low q

© 2019 WILEY-VCH Verlag GmbH & Co. KGaA, Weinheim

values (peak around 4–5 nm^{-1}), assigned to the disordered precursor-solvent colloids (see Figure S1, Supporting Information). For the $MAPbI_3$ perovskite solution (1a), the disordered sol–gel state collapses after as little as 30 s, indicated by the appearance of intense features (q = 4.4, 4.8, 6.3, and 8.1 nm^{-1}) characteristic of the $MAPbI_3 \cdot DMSO$ solvated co-crystal. Weaker scattering features associated to the presence of PbI_2 (at q = 9.0 nm^{-1}) also appear. Corresponding to this data set, Figure 1g shows the formation over time of the $MAPbI_3 \cdot DMSO$ solvate (at q = 6.3 nm^{-1}), which forms due to the strong coordination between lead and DMSO.[19] This co-crystal incorporates two DMSO molecules per unit cell, thus locking the solvent into a crystalline structure. We have previously shown that replacing triiodide with tribromide in DMF inks significantly alters the crystallization pathway for $MAPbX_3$.[21] Figure 1b illustrates that replacing triiodide with tribromide in $FAPbX_3$ inks has the same dramatic effect; the desirable 3C perovskite phase forms directly from solution. In fact, this conclusion holds for triiodides and tribromides for a wide range of cation compositions in FA-dominated cation mixtures, as shown in Figure S2 (Supporting Information). This is significant as it shows that cation mixing within this compositional range does not yield compositionally distinct phases. The direct crystallization of the 3C perovskite phase in tribromide formulations based on MA, FA, and mixed FA-MA-Cs cases can be ascribed to the stronger Pb—Br bonds than Pb-DMSO as opposed to weaker Pb—I bonds than Pb-DMSO.[33,34] Hence, lead is more completely solvated and in close interaction with DMSO in iodide formulations, whereas bromide formulations are far less solubilized by DMSO. The sol–gel colloidal state scattering is significantly more intense in the triiodide case (1c) than in the tribromide (1b) formulation, supporting the notion that there are significant differences in the Pb-DMSO complexation in the presence of these halides.[35] The slower crystallization of the sol–gel in the case of triiodides can also be related to the stronger and more prevalent Pb-DMSO complex in iodide formulations, which provides a barrier for solvent removal.

The crystallization of the $FAPbBr_3$ perovskite phase occurs after ≈50 s (Figure 1b,h), 20 s later than for the $MAPbI_3 \cdot DMSO$ case (Figure 1a,g). We ascribe this to the fact that the 3C perovskite phase is solvent-free and requires the as-cast sol–gel film to reach a higher solute concentration before initiating nucleation and growth of the 3C perovskite phase. The situation is similar for $FAPbI_3$ inks (Figure 1c), which also begin to crystallize later than $MAPbI_3$, around the ≈60 s mark, forming the nonperovskite 2H phase (q ≈ 8.5 nm^{-1}).[36] Figure 1h,i shows in greater detail the time evolutions of the $FAPbBr_3$ perovskite and 2H phases. The 2H phase forms markedly slower than the $FAPbBr_3$ phase. No other phases are formed during spin coating of $FAPbBr_3$ and $FAPbI_3$ inks.

Next, we investigated the impact of introducing a small amount of Br ($FAPbI_{2.55}Br_{0.45}$) into the $FAPbI_3$ precursor solution (Figure 1d). The addition of Br promotes the formation of another competing phase, the nonperovskite 4H phase at q ≈9.4 nm^{-1}, which partially suppresses formation of the 2H phase. The as-cast films–containing both the 2H and 4H phases ($FAPbI_{3-x}Br_x$)–appear darker than the 2H phase alone ($FAPbI_3$), as shown in the insets of Figure 1i,j and Figure S3 (Supporting Information). This suggests that the optical bandgap of the two films is somewhat different. Moreover, X-ray diffraction (XRD) analysis reveals that the 4H phase has a hexagonal structure similar to the 2H phase, but with slightly different unit cell parameters due to Br incorporation (Figure S3, Supporting Information). Importantly, the onset of crystallization of both phases is delayed to 90 s (Figure 1j). The 2H phase appears at the same q value as the triiodide 2H phase, confirming its pure iodide composition. Formation of a distinct pure triiodide 2H phase and a second mixed halide 4H-$FAPbI_{3-x}Br_x$ phase requires the active segregation of I and Br in some areas of the film. The requirement for out-diffusion of Br–whether as a precondition for nucleation or as a result of growth–provides thus a kinetic hindrance for the crystallization of both 2H and 4H phases. This significantly delays and slows their growth and also weakens their scattering signature. We ascribe the formation of two distinct phases (rather than a single mixed-halide phase) to the fact that introduction of Br influences the Pb—I—Pb bond angle, distorting the 2H structure beyond the ability of Br to incorporate into it.[34,37–40]

The introduction of additional MA^+ and Cs^+ cations into the $FAPbI_{2.55}Br_{0.45}$ precursor solution results in $FAMACsPbI_{2.55}Br_{0.45}$. This further complicates the crystallization pathway and therefore extends the lifetime of the sol–gel state (Figure 1e). The addition of Cs^+ has been argued to lower the energy barrier for forming the perovskite phase.[9,30,41] Here, we confirm it promotes the formation of the 3C perovskite phase (q ≈10 nm^{-1}). The formation of the nonperovskite 2H and 4H phases and the 3C perovskite phase are seen to be considerably delayed by ≈110 s and the scattering intensity of the three phases are generally weak (Figure 1k and inset thereof). Simultaneous addition of Cs^+ and Br is required to promote the formation of the perovskite phase, which appears to be an entropically stabilized perovskite phase.[42] Nevertheless, there is evidence of competition between three distinct crystalline phases, which requires diffusion and segregation of precursors. This results in further delays in the formation of the byproduct phases, preserving the sol–gel state a little longer.

We have sought to verify this hypothesis by addition of Rb^+ to the above mixed cation/mixed halide formulation, which indeed is found to further extend the sol–gel lifetime (Figure 1l). The addition of Rb^+ promotes the formation of an additional solvate phase (S). This is a fourth phase and it likely requires cation and/or halide segregation to occur in order to form. The crystallization is therefore further delayed by a whopping 2 min, which puts the onset of crystallization at the 4 min mark.

We summarize the above observations by classifying the crystallization kinetics and diffraction intensities for the range of FA-rich formulations to yield one, two or three crystalline byproducts. **Figure 2**a shows the scattering intensity versus q at the very end of solution-casting for triiodide perovskites based on FA- ($FAPbI_3$) and FA-dominated mixed-cation formulations ($FAMAPbI_3$, $FACsPbI_3$, and $FAMACsPbI_3$). All four formulations collapse at approximately the same time into the 2H crystalline phase (q = 8.5 nm^{-1}, Figure 2b). Given the appearance of a single 2H phase at the same q value, the same onset and approximate rate of crystallization, and the same final diffraction intensities, we conclude that the 2H phases incorporate the minority cations (MA^+ and Cs^+), resulting, most likely, in

© 2019 WILEY-VCH Verlag GmbH & Co. KGaA, Weinheim

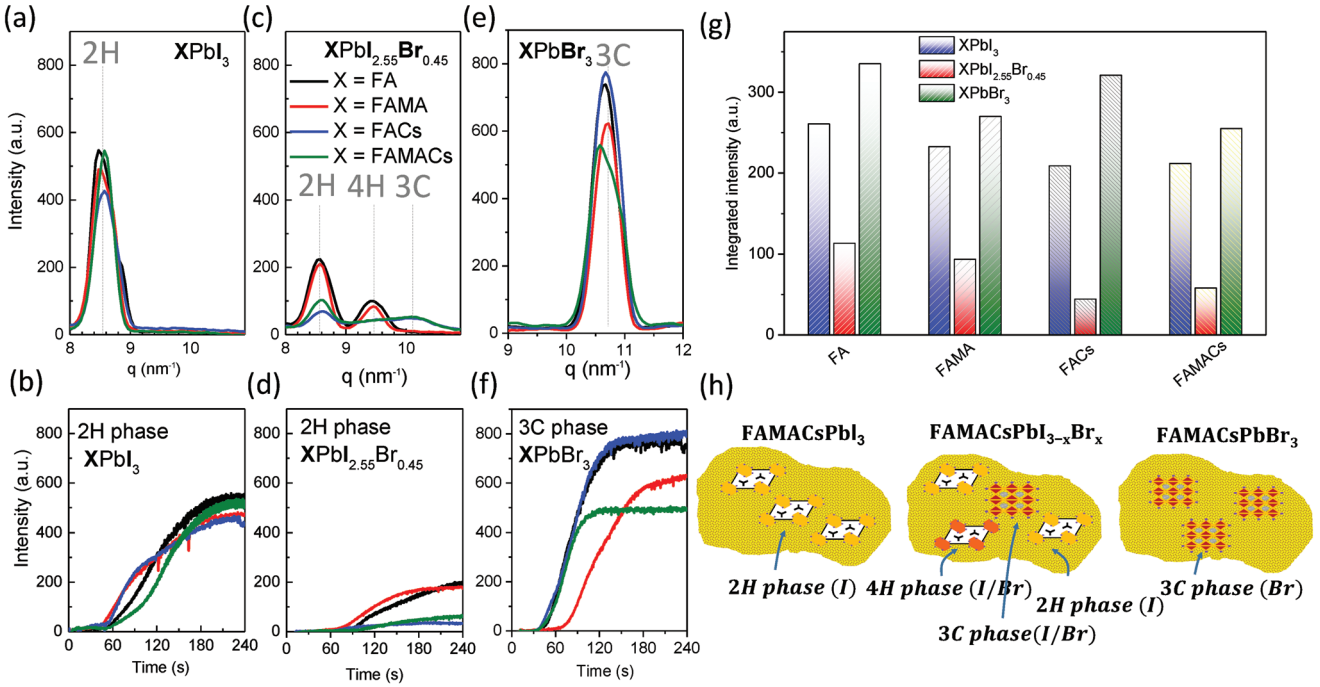

Figure 2. In situ GIWAXS intensity plots of crystallization byproducts for triiodide, tribromide, and mixed iodide-bromide FA-dominated hybrid perovskite inks at the end of spin coating. a) Scattering intensity versus q at final spin-coating stage and b) intensity versus time of 2H-phase for FA-based triiodide perovskites prepared with different cation compositions. c) Scattering intensity versus q at final spin-coating stage and d) intensity versus time of 2H-phase for FA-based mixed halide perovskites prepared with different cation compositions. e) Scattering intensity versus q at final spin-coating stage and f) intensity versus time of 3C-phase for FA-based tribromide perovskites prepared with different cation compositions. g) Total integrated intensity of all crystalline byproducts based on triiodide, tribromide and mixed halide compositions. h) Schematic representation of phase segregation.

mixed-cation hexagonal phases: 2H-$FAMAPbI_3$, 2H-$FACsPbI_3$, and 2H-$FAMACsPbI_3$ (Figure 2h). This conclusion is supported by the absence of a distinct $MAPbI_3 \cdot DMSO$ solvate phase and by the absence of a distinct perovskite phase when Cs^+ is added.

The situation is markedly different for FA-dominated mixed-halide films (Figure 2c). As described above, $FAPbI_{2.55}Br_{0.45}$ shows evidence of two distinct crystalline phases: 2H ($q = 8.5\ nm^{-1}$) and 4H ($q = 9.4\ nm^{-1}$). Addition of a small amount of MA yields $FAMAPbI_{2.55}Br_{0.45}$ with two identical peaks as $FAPbI_{2.55}Br_{0.45}$. However, the incorporation of a small amount of Cs^+ ($FACsPbI_{2.55}Br_{0.45}$ and $FAMACsPbI_{2.55}Br_{0.45}$) leads to a further significant reduction of the intensities of the 2H and 4H phases and promotes the perovskite 3C phase (Figure 2h). This result indicates that the entropically stabilized perovskite phase requires both Cs^+ and Br addition to iodide to form spontaneously and not only the mixed cations or mixed halides, suggesting thereby the synergistic effects of Cs and Br. Addition of Rb^+ together with Cs^+ once again promotes formation of a solvated (S) phase, as shown in Figure 1.

The tribromide systems yield exclusively the 3C perovskite phase for all FA-dominated cation compositions (Figure 2e). Commensurately, we find that crystallization in most cases occurs early (≈30–35 s) and rises rapidly. The addition of MA^+ appears to delay and weaken the crystallization of the perovskite phase, whereas Cs^+ does not. Simultaneous addition of MA^+ and Cs^+ does not perturb the perovskite formation kinetics, but the total intensity is somewhat reduced, compared to the pure FA case. This suggests that MA^+ somewhat perturbs the crystallization process, albeit without altering the phases formed, unless Rb^+ is added to the system. In the latter case MA^+ segregates to form an additional solvated phase, as shown in Figure 1, which further delays sol–gel collapse.

The formation kinetics of one-, two-, and three-phase systems (Figure 2b,d,f) exhibiting different compositions show once again the compelling link between the number of crystalline byproducts and the onset and rate of growth. The integrated diffraction intensity of these phases in mixed-halide formulations (resulting in two or more phases) is significantly lower than in the triiodide and tribromide cases (where only one phase formed, Figure 2g). This strongly points to a reduced overall crystalline volume in the as-cast film due to kinetic hindrance for the growth of multiple halide and/or cation segregated phases. Such growth requires mass transport of precursors to their associated phases. Representative 2D GIWAXS snapshots taken of various perovskite compositions at the final stage of spin coating (at 240 s) are shown in Figure S4 (Supporting Information).

The temporal evolution of the sol–gel state itself (leading up to the crystallization) deserves closer examination in the presence of different halides. We decided to compare the effect of halide composition in the context of FA-dominated mixed-cation systems: $FAMACsPbBr_3$, $FAMACsPbI_3$, and $FAMACsPbI_{2.55}Br_{0.45}$. In situ UV–vis transmittance/absorbance measurements were performed during spin-coating to complement the in situ GIWAXS data and to monitor the solution thinning and absorbance change. Comparing the colloidal sol–gel scattering intensities of $FAPbI_3$ and $FAPbBr_3$ (Figure 1b,c) already revealed that the former system exhibits

© 2019 WILEY-VCH Verlag GmbH & Co. KGaA, Weinheim

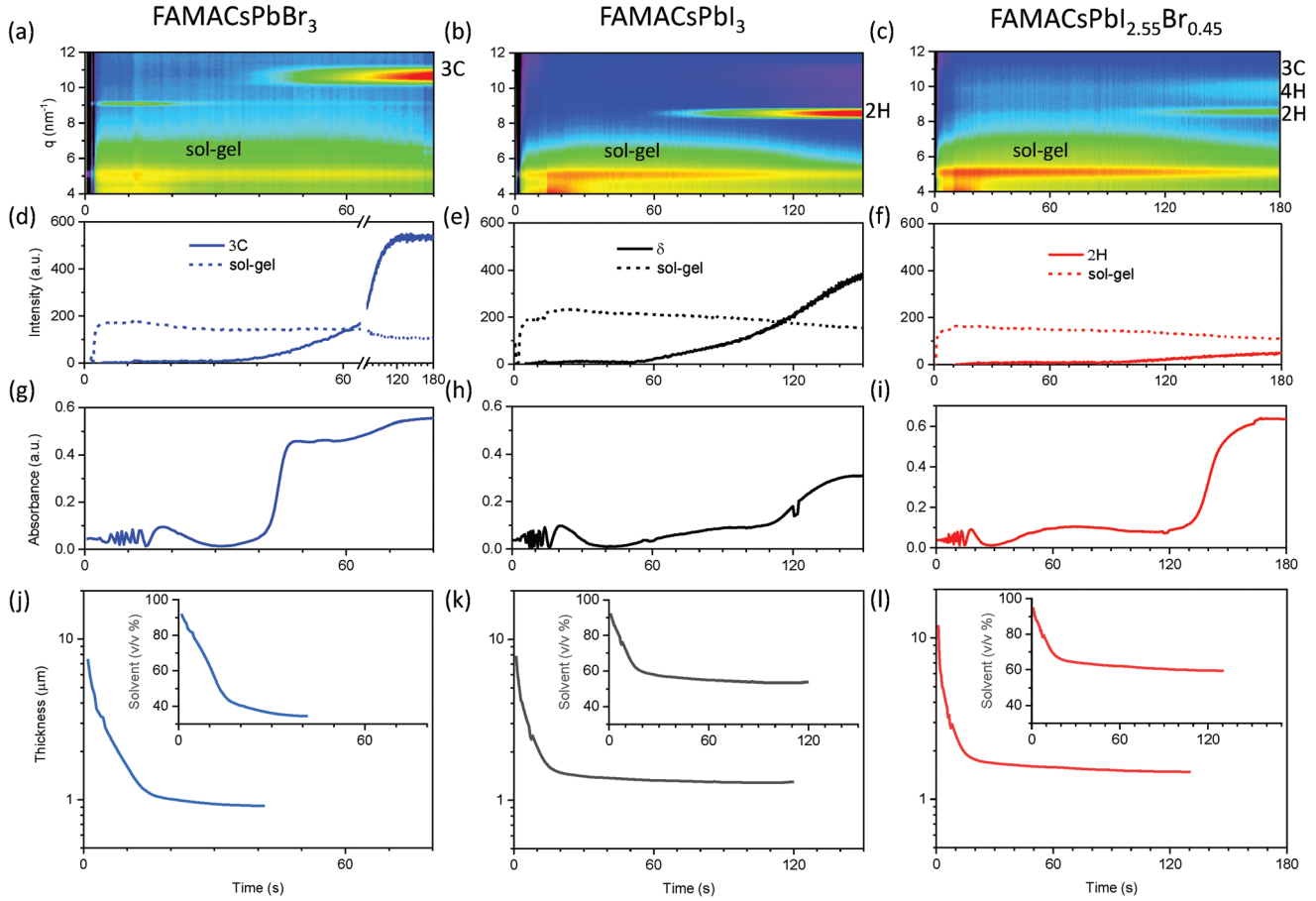

Figure 3. Time-evolution of the as-cast sol–gel film of $FA_{0.81}MA_{0.14}Cs_{0.05}PbX_3$ (FAMACsPbX$_3$) based on different halides (X = I, Br, and $I_{0.85}Br_{0.15}$). a–c) Time-resolved GIWAXS intensity maps showing the ink-to-solid transformation during spin coating of the following perovskite precursor inks: a) FAMACsPbBr$_3$, b) FAMACsPbI$_3$, and c) $FAMACsPbI_{2.55}Br_{0.45}$. d–f) Intensity versus time for: d) FAMACsPbBr$_3$ formulation (sol–gel phase and 3C-phase), e) FAMACsPbI$_3$ formulation (sol–gel phase and 2H-phase), and f) $FAMACsPbI_{2.55}Br_{0.45}$ (sol–gel phase and 2H-phase). g–i) Time evolution of absorbance at 550 nm during spin coating of: g) FAMACsPbBr$_3$, h) FAMACsPbI$_3$, and i) $FAMACsPbI_{2.55}Br_{0.45}$ formulations. j–l) Thinning behaviors of spin-cast solutions of: j) FAMACsPbBr$_3$, k) FAMACsPbI$_3$, and l) $FAMACsPbI_{2.55}Br_{0.45}$ formulations. Insets show the calculated volume fraction of solvent in the as-cast sol–gel film, based on the final dry film thickness.

stronger scattering and a more sustained sol–gel state than the latter. This behavior is also observed in mixed-cation tribromide (**Figure 3**a,d) and triiodide (Figure 3b,e) precursor solutions. In situ absorbance measurements (Figure 3g,h) confirm that the formation onset of the darker 3C perovskite phase (tribromide) and 2H phase (triiodide) within the disordered and optically transparent sol–gel state is accompanied by an expected increase in optical absorbance. The optical interference oscillations during the early stages of spin coating reflect the rapid thinning of the solution. Their quantitative analysis yields the temporal thickness evolution for the three formulations (Figure 3j,k,l). In all three cases, an initial wet-film thickness of ≈8–10 µm is measured, rapidly thinning within the first 15 s to a ≈1–2 µm solvated film, which we call the sol–gel film. This marks a transition from a solution-thinning behavior (dominated by outflow and evaporation) to sol–gel thinning (dominated by solvent-lead complexes within the sol–gel film). Thus, the decomposition of lead-solvent complexes dictates the effective evaporation rate of the solvent. The sol–gel film retains a volume fraction as high as ≈60% (65%) of solvent compared to the thermally annealed film in the triiodide (mixed halide) case. The solvent volume fraction is much lower (≈45%) in the tribromide case. Commensurately, the sol–gel film thins at a higher rate of 0.63 µm s^{-1} in the tribromide case, slowing down to 0.52 and 0.48 µm s^{-1} in the triiodide and mixed halide cases, respectively. The differences in initial solvation of the sol–gel film and solvent loss rate at room temperature reflect the expectation of weaker lead-solvent interactions in the presence of bromine and stronger lead-solvent interactions in the presence of iodide. We note that the halide mixture thins more slowly than pure-halide formulations pointing to unexpected synergistic effects due to a small addition of Br. Further in-depth investigation of the sol–gel chemistry is beyond the scope of this study. However, the literature provides useful clues as to the possible origin of sol–gel collapse. X-ray scattering and UV–vis absorbance studies of lead halide solutions have revealed formation of lead-solvent complexes known as iodiplumbates and bromoplumates with the former more susceptible to formation of lead-solvent complexes than the latter.[43,44] Indeed, lead bromide tends to

© 2019 WILEY-VCH Verlag GmbH & Co. KGaA, Weinheim

complex more weakly with polar solvents and therefore forms metal-rich clusters, whereas lead iodide complexes with DMSO (strongly) and DMF (moderately),[45] and is in fact known to form PbI_2-solvent and $MAPbI_3$-solvent co-crystalline phases with both DMSO and DMF.[21,46,47] No such phases have been observed with $PbBr_2$ or with $FAPbI_3$, indicating the importance of halide and cation compositions to determining the sol–gel chemistry. During slow drying of the as-cast solution, the sol–gel precursor film containing a mixture of lead iodide and lead bromide in the presence of DMSO and DMF will see solvent molecules preferentially complexed with iodide-bound lead and is therefore less likely to evaporate. Meanwhile, the solvent can more easily evaporate when interacting with bromide-bound lead. This heterogeneous removal of solvent from the sol–gel enriches iodide-rich areas with solvent as compared to bromide-rich regions and can drive clustering of the sol–gel colloids. With the preferential loss of solvent in Br-rich regions, supersaturation promotes nucleation and growth of nonperovskite intermediate phases, including iodide-rich solvates, PbI_2 and Br-rich hexagonal phases. This proposed mechanism may explain why the sol–gel state appears to collapse into halide segregated phases from an otherwise uniform mixture of components instead of forming the entropically more stable mixed halide mixed cation perovskite phase.

To elucidate the effect of the CB drip on the sol–gel state, we have monitored in situ spin-coating of $FAPbI_3$ and $FAMACsPbI_{2.55}Br_{0.45}$ formulations with CB drip at 20 s. **Figure 4**a shows the time-evolution of the scattering intensity distribution during spin-coating of the $FAPbI_3$ perovskite precursor. An intense scattering feature associated to the 2H phase is formed immediately upon CB dripping at 20 s. Comparison of the crystallization kinetics of the 2H phase with and without CB dripping reveals the dramatic effect of the drip (Figure 4b), which is to nucleate and grow this crystalline phase almost instantaneously. The CB drip promotes the nucleation and growth by removing the complexed solvent from within the sol–gel film. The case of the mixed-cation mixed-halide $FAMACsPbI_{2.55}Br_{0.45}$ precursor solution is shown in Figure 4c–f. Here too, the CB drip promotes the abrupt formation of the 2H phase at first, but this quickly gives way to formation of the 3C perovskite phase (Figure 4d). This appears to consume or convert the 2H phase into the perovskite phase, increasing the sample's absorbance following the drip (Figure 4e). This "competitive" crystallization process between 3C and 2H phases is likely the result of the synergetic effect of combining Br and Cs to form an entropically stabilized 3C perovskite phase, which is favored over the 2H phase at room temperature. The formation of the crystalline phases upon CB drip testifies the collapse of the sol–gel state. This is clearly indicated by the weakening of the sol–gel scattering signal (Figure 4a,c) as traced in Figure 4f for the mixed-halide mixed-cation case. Whereas the sol–gel signal weakens significantly, consistent with the requirement for the formation of solvent-free crystalline phases, it does not disappear entirely. Rather, it continues to weaken as the remaining solvent evaporates through decomposition of the lead-solvent complexes. Inferred from the XRD of the $FAPbI_3$ and $FAMACsPbI_{2.55}Br_{0.45}$ films shown in Figure S5 (Supporting Information), upon CB drip and thermal annealing at 100 °C for 30 min, the dynamic conversion behavior of $FAPbI_3$ is the gradual increase of the intensity of 2H phase, while $FAMACsPbI_{2.55}Br_{0.45}$ undergoes conversion to the 3C (3R) phase directly.[34] Temperature-dependent XRD of these films are shown in Figure S6 (Supporting Information). It's clear that the 3C (100) phase is already present in the case of the as-cast $FA_{0.81}MA_{0.14}Cs_{0.05}PbI_{2.55}Br_{0.45}$ film but is not formed until annealing to ≈125 °C in the case of the $FAPbI_3$ film. This result confirms the facile in situ formation of the desired 3C phase in the mixed halide formulation, in agreement with a recent study comparing the in situ and thermal conversions of various mixed halide mixed cation perovskites.[48]

Our study so far revealed that the disordered sol–gel state of the as-cast film can be stabilized and its longevity extended substantially from several seconds, in the case of $MAPbI_3$, to several minutes in the mixed-halide mixed-cation case. This broadens the processing window of perovskites and facilitates their reproducible fabrication. We now test the impact of these findings by fabricating a large number of PSCs using formulations which have demonstrated rapid ($MAPbI_3$), intermediate ($FAMACsPbI_3$), and slow ($FAMACsPbI_{2.55}Br_{0.45}$ and $FAMACsRbPbI_{2.55}Br_{0.45}$) collapses of the sol–gel film. We varied the CB drip timing as main parameter in the fabrication of n–i–p devices (glass/indium tin oxide (ITO)/TiO_2/perovskite/spiro-MeOTAD/Au). The device parameters for each formulation and all dripping times are summarized in Table S1 (Supporting Information). Representative *J*–*V* curves are shown in Figure S7 (Supporting Information). In **Figure 5**e–h we have plotted the PCE of solar cell devices made from different formulations with respect to the dripping time, along with the time-evolution of the GIWAXS data showing the structural evolution of the sol–gel film (Figure 5a–d). Figure S8 (Supporting Information) gives the statistics of FF, J_{sc}, and V_{oc} of $FAMACsPbI_3$ and $FAMACsPbI_{2.55}Br_{0.45}$ devices. The results clearly show how the CB processing window for high-efficiency PSCs coincides with the time window during which the sol–gel film is formed (>15 s) and remains disordered. In the case of $MAPbI_3$, the drip must therefore occur within 20–30 s, preceding the formation of the solvated crystalline phase. In the case of $FAMACsPbI_3$, the processing window is restricted by the nucleation of the 2H phase at ≈60 s. Next, in the $FAMACsPbI_{2.55}Br_{0.45}$ case, the processing window closes at ≈120 s, matching the formation of the crystalline phases. Finally, in the $FAMACsRbPbI_{2.55}Br_{0.45}$ case, the processing window closes at 160–200 s, just before the crystalline phase forms. The processing window ends abruptly with the nucleation and growth of the crystalline phases of the $MAPbI_3$ and $FAMACsPbI_3$ formulations. PSCs made from films with a too late drip simply do not work. The processing window ends less drastically for $FAMACsPbI_{2.55}Br_{0.45}$ and $FAMACsRbPbI_{2.55}Br_{0.45}$, and even devices made without drip appear to work, but with PCEs not higher than 6%. Dripping at early times, i.e., prior to formation of the sol–gel film yields poor PCE. This is consistent with our prior observation that thermal conversion of the as-cast film, when still in the liquid phase, yields films with poor morphology.[21] We generally find that dripping at ≈20 s yields the best performance for the three FA-dominated formulations, with PCE = 17.8%, J_{sc} = 22.4 mA cm^{-2}, V_{oc} = 1.10 V, and FF = 72.3% for $FAMACsPbI_3$, PCE = 20.4%, J_{sc} = 23.3 mA cm^{-2}, V_{oc} = 1.15 V, and

© 2019 WILEY-VCH Verlag GmbH & Co. KGaA, Weinheim

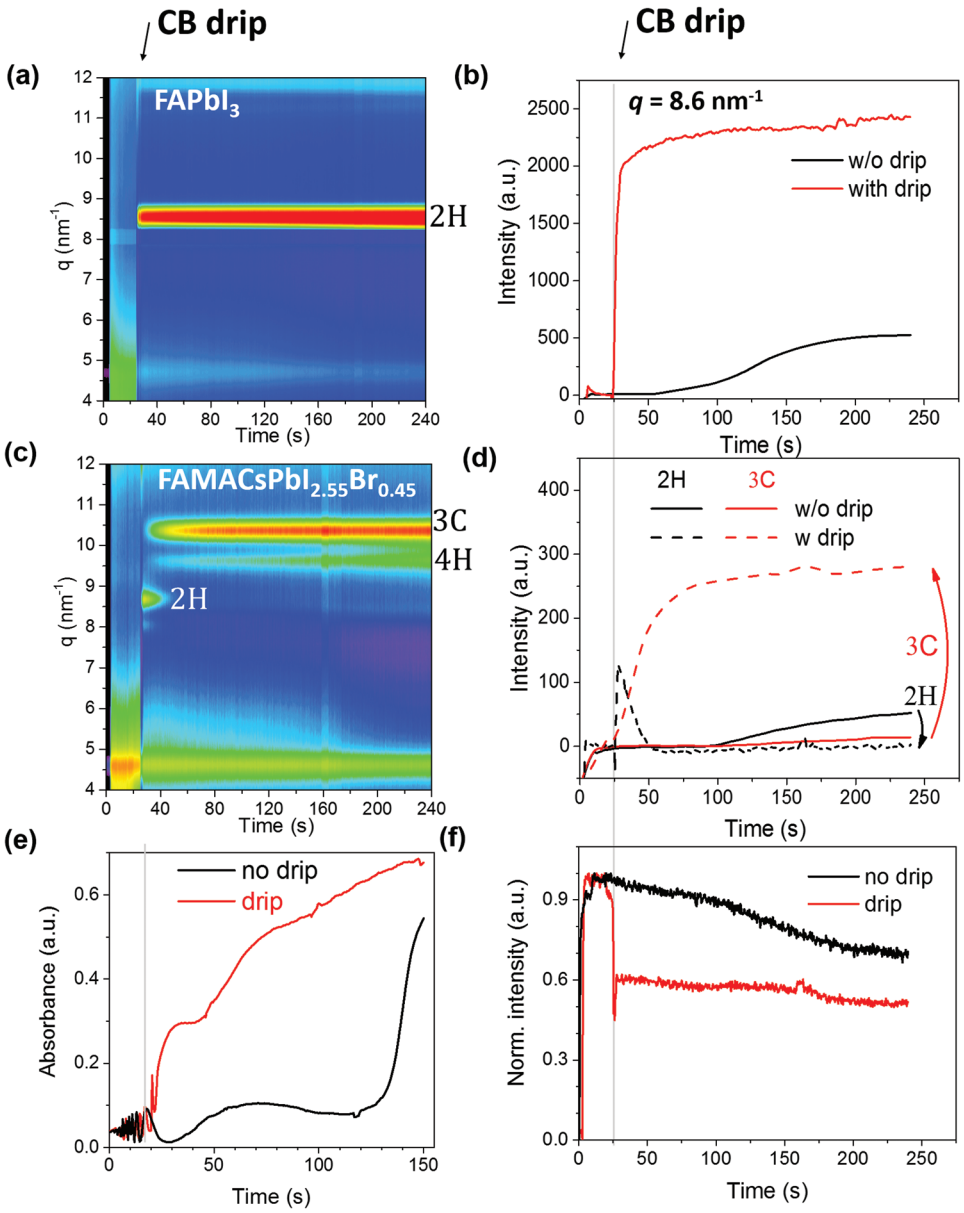

Figure 4. a,c) In situ 2D GIWAXS intensity map of: a) $FAPbI_3$ and c) $FAMACsPbI_{2.55}Br_{0.45}$ precursors with CB anti-solvent drip around 20 s during spin coating up to 240 s. b,d) Time evolution of the diffraction intensity related to 2H phase (q = 8.5 nm^{-1}) and perovskite 3C phase (q = 10.1 nm^{-1}) for perovskite: b) $FAPbI_3$ and d) $FAMACsPbI_{2.55}Br_{0.45}$, respectively. e) Time evolution of absorbance at 550 nm during spin coating without and with anti-solvent drip for $FAMACsPbI_{2.55}Br_{0.45}$ perovskite. f) Intensity versus time (q = 5.1 nm^{-1}) for $FAMACsPbI_{2.55}Br_{0.45}$ perovskite.

FF = 76.5% for $FAMACsPbI_{2.55}Br_{0.45}$, and PCE = 20.0%, J_{sc} = 23.1 mA cm^{-2}, V_{oc} = 1.14 V, and FF = 75.3% for $FAMACsRbPbI_{2.55}Br_{0.45}$. Representative reverse and forward J–V scans, external quantum efficiency (EQE) measurements and steady-state photocurrent of $FAMACsPbI_{2.55}Br_{0.45}$ dripped at 40 s are shown in Figure S9 (Supporting Information). The integrated J_{sc} from the EQE spectra yielded J_{sc} values of 21.1 mA cm^{-2}, in good agreement with those obtained from J–V measurements. The slow decrease of PCE for later drip times within the sol–gel window is due to slight reductions of the FF and J_{sc}. The PCE is maintained above 16% even for a drip time of 100 s, but the loss in efficiency suggests that the perovskite-film formation and morphology are still somewhat sensitive to the slowly changing composition of the disordered sol–gel film, which may undergo nanoscale halide segregation, detrimental to the overall perovskite-film quality. We also do not exclude the possibility that the effectiveness of CB dripping changes with the decreasing solvation level of the as-cast sol–gel film, making the spontaneous crystallization of the perovskite phase less effective.

Overall, the impact of CB dripping outside the sol–gel window is clearly seen by examining the scanning electron microscopy (SEM) images of films formed at different drip times (Figure 5i–l). $MAPbI_3$ films prepared with drip while

© 2019 WILEY-VCH Verlag GmbH & Co. KGaA, Weinheim

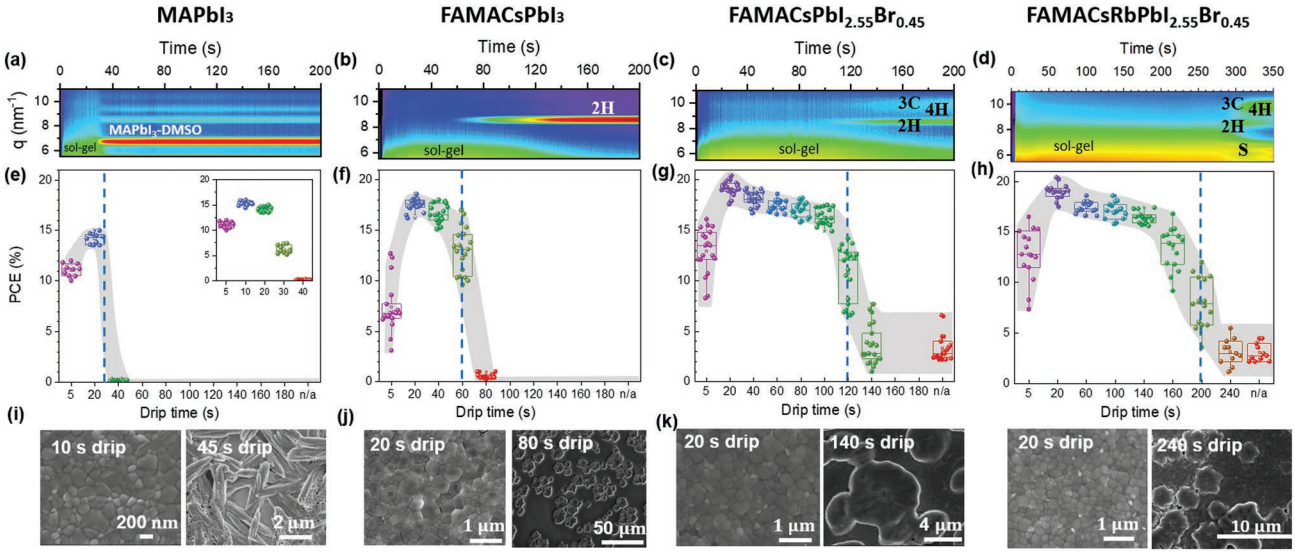

Figure 5. a–d) In situ 2D GIWAXS intensity maps plot of: a) $MAPbI_3$, b) $FAMACsPbI_3$, c) $FAMACsPbI_{2.55}Br_{0.45}$, and d) $FAMACsRbPbI_{2.55}Br_{0.45}$. e–h) PCE statistical distribution of solar cells with varied dripping time for: e) $MAPbI_3$, f) $FAMACsPbI_3$, g) $FAMACsPbI_{2.55}Br_{0.45}$, and h) $FAMACsRbPbI_{2.55}Br_{0.45}$, results are shown for 20 cells for each condition. i–l) SEM images of the perovskite film with varied dripping time for: i) $MAPbI_3$, j) $FAMACsPbI_3$, k) $FAMACsPbI_{2.55}Br_{0.45}$, and l) $FAMACsRbPbI_{2.55}Br_{0.45}$.

the sol–gel film is disordered (10 s) result in a compact film, whereas dripping after the solvated co-crystal forms (45 s) results in bad quality films, full of pinholes. Similar behavior is seen for the other systems, whereby a late drip results in isolated domains and pinholes. The film coverage is greater in the mixed-cation case, in agreement with the devices which showed functional, albeit inefficient solar cells even with very late or no anti-solvent drip. The extended longevity of the sol–gel state, even after crystallization begins, provides a buffer against the complete collapse of the as-cast film into isolated domains and allows formation of sufficiently high quality films to yield working solar cells. These results highlight the importance of the sol–gel state of the film and its role in maintaining the integrity and continuity of polycrystalline thin films. It is nevertheless apparent that early drip is preferred to later drip, even within the sol–gel stabilization window. This is explained by the likelihood that anti-solvent drip performed early quenches the sol–gel from a well-mixed state to form the mixed perovskite phase, whereas dripping later implies quenching a slightly more segregated sol–gel state where iodide- ad bromide-rich components have begun to cluster by virtue of differences in their interaction strength with the solvent.

Overall, we revealed that Rb^+ and Cs^+ addition can extend the sol–gel state lifetime, which in turn results in a wider anti-solvent processing window to achieve high-quality perovskite films. Recently, K^+ addition was also shown to be beneficial to obtain high-performance PSCs with suppressed hysteresis, partially due to a passivation effect.[49–51] Given that K^+ is similar to Rb^+, we expect that added K^+ might affect the sol–gel lifetime as well and likely exhibits a very wide processing window as well, explaining the robustness and reproducibility of device fabrication process.

We have systematically investigated a series of perovskite formulations with increasing compositional complexity by in situ time-resolved GIWAXS and optical absorbance measurements. In doing so, we elucidated the importance of the sol–gel state formed during solution casting, the prevention of its premature collapse and the intricacies in triggering its conversion to the desirable perovskite phase. We showed, for instance, that replacing MA with FA changes the nature of the intermediate crystalline phase from an ordered solvated phase forming within 30 s ($MAPbI_3$) to a 2H phase which forms within 60 s due to the requirement for solvent removal. A small amount of Br added to the formulation suppresses this 2H phase and promotes the formation of a competing mixed-halide 4H phase. Meanwhile, addition of Cs promotes the formation of the entropically-stabilized $FAMACsPbI_{2.55}Br_{0.45}$ perovskite by competing with the other two phases. This results in the formation of three phases after as much as 2 min. The sol–gel lifetime can be further extended to 4 min by adding a small amount of Rb^+. We showed that anti-solvent dripping within the sol–gel window is crucial to achieve high-quality films. The drip has the benefit of self-selecting formation of the perovskite phase in the $FAMACsPbI_{2.55}Br_{0.45}$ case, but not in triiodide cases. Informed by these findings, we showed that solar cell performance is far less sensitive to the drip timing as long as it is performed within the sol–gel state of the as-cast film, in agreement with our predictions from in situ GIWAXS studies. This study points to new directions in the development of perovskite formulations that can further stabilize the sol–gel state and promote its controlled and direct conversion to the desirable perovskite phase and microstructure. This is critical in achieving better performing, reproducible, cost-efficient, and scalable manufacturing of hybrid perovskite solar cells.

Experimental Section

Perovskite Solution Preparation: The organic cation salts methylammonium iodide (MAI), formamidinium iodide (FAI),

© 2019 WILEY-VCH Verlag GmbH & Co. KGaA, Weinheim

methylammonium bromide (MABr), and formamidinium bromide (FABr) were purchased from Dyesol, the lead halide compounds (PbI_2, $PbBr_2$) from Sigma-Aldrich, and CsI is from Alfa Aesa. Spiro-MeOTAD was purchased from Xi'an Polymer Light Technology Cory. All chemicals were used without further purification. All perovskite precursor 1.2 M solution was prepared and kept overnight at 60 °C with stirring, followed by filtering by 0.45 µm PTPE filter before usage. For example, the $FA_{0.81}MA_{0.14}Cs_{0.05}PbI_{2.55}Br_{0.45}$ precursor solution (1.2 M) was prepared in a molar ratio of PbI_2/$PbBr_2$ and FAI/MABr both fixed at 0.85:0.15, and the molar ratio of CsI/(FAI+MABr) at 0.05:0.95, the molar ratio of (FAI+MABr+CsI)/(PbI_2+$PbBr_2$) was 1:1. The TiO_2 nanocrystal solutions is prepared as per the literature.[52,53]

Substrate Preparation: All substrates were cleaned by sequential sonication in soap, acetone, and ethanol for ≈20 min and followed by 15 min of UV–ozone exposure. For GIWAXS measurements, polished glass (1 cm × 1 cm) substrates (Sigma Aldrich) were coated with two layers of TiO_2 to mimic the cell fabrication; patterned ITO glass substrates (2.5 cm × 2.5 cm) were used for solar cell fabrication and for obtaining SEM images; All the GIWAXS experiments were conducted on TiO_2 coated glass substrate. The TiO_2 nanocrystal solutions were spin-coated on glass substrate and annealed on a hot plate at temperature of 150 °C for 30 min in ambient air. The thickness of TiO_2 was about 50 nm. For solar cell devices, glass was taken replaced by pre-patterned indium tin oxide (ITO) glass substrate and residue procedure keep the same.

Grazing-Incidence Wide-Angle X-Ray Scattering: GIWAXS measurements were conducted at Cornell High Energy Synchrotron Source (CHESS) on the D1 beam line. Spin-coating experiments were conducted at a custom-built spin-coating stage with splashing of solvent protected using kapton tape and controlled from the computer outside the hutch. A 0.5 mm × 0.1 mm monochromated X-ray beam (double-bounce multilayer monochromator) with a wavelength of 1.16 Å (10.6 keV) was used. GIWAXS data was collected with a Pilatus 200k pixel array detector (Dectris, Baden-Dättwil, Switzerland; 100 frames per second) placed at ≈173 mm away from the sample. To balance between time resolutions and signal quality, an incidence angle of 0.25° with respect to the substrate plane and an exposure time of 0.2 s were employed. As the X-ray hutch needs closing prior to data collection, there is an estimated ≈15 s delay between solution casting and the start of spin-coating and simultaneous GIWAXS measurements. Fit2D software was used to analyze the images data, followed by using Originlab to plot the graphs. The intensity maps are color-coded using the rainbow pallet. Mathematically, q is equal to $4\pi\sin\theta/\lambda$, where θ denotes the total scattering angle multiplied by 0.5 and λ is the wavelength of the X-rays used for the measurement. The detector used for the measurement was actually a combination of two 100 K detectors. The solutions were prepared in a N_2 glove box with moisture levels below 0.1 ppm and were taken out in ambient environment right before the experiment. Thin films perovskite were deposited by spin coating at 2000 rpm for 10 s (20 s for Rb case) and 4000 rpm for 230 s. All the experiments were conducted in an ambient atmosphere where the relative humidity was ≈20–25%.

Solar Cell Device Fabrication and Characterizations: The solar-cell devices were fabricated using TiO_2 thin-film procedure on patterned ITO-coated glass. Perovskite solutions were spin coated on top of the TiO_2 layer at 2000 rpm for 10 s with an acceleration of 200 rpm s^{-1}. The second step was 4000 rpm for needed time with a ramp-up of 1000 rpm s^{-1}. Chlorobenzene (0.1 mL) was dropped on the spinning substrate during the second spin-coating step at 10 s before end of the procedure. The films were then annealed at 100 °C for 10 min. After cooling down to room temperature, the hole-transporting layer was then deposited on top of the perovskite film via spin-coating at 4000 rpm for 30 s using a chlorobenzene of a 80 mg mL^{-1} solution of 2,2′,7,7′-tetrakis-(*N*,*N*-di-pmethoxyphenylamine) 9,9′-spirobifluorene (spiro-MeOTAD), with additives of lithium bis(trifluoromethanesulfonyl) imide and 4-*tert*-butylpyridine. Finally, 80 nm of gold electrodes were deposited by thermal evaporation using an Angstrom evaporator. The current-density–voltage (*J–V*) curves were measured inside the nitrogen-filled glovebox by employing ABET solar simulator system with an illumination intensity of 1000 mW cm^{-2} (AM 1.5G), as checked with a calibrated reference solar cell (RERA Technologies).The *J–V* curves of cells were obtained by Keithley 2400 source, on an active area of 10 mm^2 for each pixel, without any pre-conditioning, at a scan rate of 380 mV s^{-1} in the voltage range from −0.1 to 1.2 V. The reversed scan (from 1.2 to −0.1 V) was reported for device comparison. It was noted that there is still a ≈5–10% hysteresis associated with all the solar cells.

In Situ UV–Vis Transmission/Reflection Measurements during Spin Coating: UV–vis transmission/reflection measurements were performed using a F20-UVX spectrometer with a tungsten halogen light source (Filmetrics, Inc.) with a repetition rate of 10 Hz and an integration time of 0.1 s for each spectrum during spinning. These measurements were conducted in a N_2 glove box with moisture level below 0.1 ppm, using the following equation: $A_\lambda = -\log_{10}(T)$, where A_λ is the absorbance at a certain wavelength (λ) and T is the calibrated transmitted radiation. Temperature-dependent XRD was carried out using an X-ray diffractometer (Empyrean, PANalytical, Almelo, The Netherlands) equipped with a N_2-filled heating chamber. The as-cast films (with chlorobenzene drip) were heated at the rate of 3 °C min^{-1} from room temperature to 150 °C, XRD patterns are collected at every 6 °C increment.

Thin-Film Characterization: A Nikon LV-100 optical microscope was used to obtain the optical microscopy images. SEM images were taken using Nano-SEM with in-lens detector using a 10 kV accelerating voltage and a 5 mm working distance. XRD spectra of perovskite films were obtained at Brucker D8 from 10° to 45° with a scan rate of 3° min^{-1} (X-ray source: Cu Kα, λ = 1.54 Å).

Supporting Information

Supporting Information is available from the Wiley Online Library or from the author.

Acknowledgements

K.W. and M.-C.T. contributed equally to this work. The research reported in this publication was supported by funding from King Abdullah University of Science and Technology (KAUST) Office of Sponsored Research (OSR) under award no. OSR-CARF URF/1/3079-33-01. CHESS is supported by the NSF award DMR-1332208. Temperature-dependent XRD measurements were performed in part at the Analytical Instrumentation Facility (AIF) at North Carolina State University, which is supported by the State of North Carolina and the NSF award no. ECCS-1542015.

Conflict of Interest

The authors declare no conflict of interest.

Keywords

anti-solvent drip, hybrid perovskite solar cells, in situ GIWAXS, kinetic stabilization, mixed-cation mixed-halide perovskites

Received: December 28, 2018
Revised: May 23, 2019
Published online:

[1] W. S. Yang, B.-W. Park, E. H. Jung, N. J. Jeon, Y. C. Kim, D. U. Lee, S. S. Shin, J. Seo, E. K. Kim, J. N. Noh, S. I. Seok, *Science* **2017**, *356*, 1376.

© 2019 WILEY-VCH Verlag GmbH & Co. KGaA, Weinheim

[2] N. J. Jeon, J. H. Noh, W. S. Yang, Y. C. Kim, S. Ryu, J. Seo, S. I. Seok, *Nature* **2015**, *517*, 476.
[3] A. Kojima, K. Teshima, Y. Shirai, T. Miyasaka, *J. Am. Chem. Soc.* **2009**, *131*, 6050.
[4] N. J. Jeon, H. Na, E. H. Jung, T.-Y. Yang, Y. G. Lee, G. Kim, H.-W. Shin, S. Seok, J. Lee, J. Seo, *Nat. Energy* **2018**, *3*, 682.
[5] D. Luo, W. Yang, Z. Wang, A. Sadhanala, Q. Hu, R. Su, R. Shivanna, G. Trindade, J. Watts, Z. Xu, T. Liu, K. Chen, F. Ye, P. Wu, L. Zhao, J. Wu, Y. Tu, Y. Zhang, X. Yang, W. Zhang, R. H. Friend, Q. Gong, H. J. Snaith, R. Zhu, *Science* **2018**, *360*, 1442.
[6] W. Chen, Y. Wu, Y. Yue, J. Liu, W. Zhang, X. Yang, H. Chen, E. Bi, I. Ashraful, M. Gratzel, L. Han, *Science* **2015**, *350*, 944.
[7] S. D. Wolf, J. Holovsky, S. J. Moon, P. Loper, B. Niesen, M. Ledinsky, F. Haug, J. H. Yum, C. Ballif, *J. Phys. Chem. Lett.* **2014**, *5*, 1035.
[8] M. Saliba, T. Matsui, K. Domanski, J. Y. Seo, A. Ummadisingu, S. M. Zakeeruddin, J. P. Correa-Baena, W. R. Tress, A. Abate, A. Hagfeldt, M. Gratzel, *Science* **2016**, *354*, 206.
[9] M. Saliba, T. Matsui, J.-Y. Seo, K. Domanski, J. P. Correa-Baena, M. K. Nazeeruddin, S. M. Zakeeruddin, W. Tress, A. Abate, A. Hagfeldt, M. Gratzel, *Energy Environ. Sci.* **2016**, *9*, 1989.
[10] M. Abdi-Jalebi, Z. Garmaroudi, A. Pearson, G. Divitini, S. Cacovich, B. Philippe, H. Rensmo, C. Ducati, R. H. Friend, S. D. Stranks, *ACS Energy Lett.* **2018**, *3*, 2671.
[11] J. Li, R. Munir, Y. Fan, T. Niu, Y. Liu, Y. Zhong, Z. Yang, Y. Tian, B. Liu, J. Sun, D. Smilgies, S. Thoroddsen, A. Amassian, K. Zhao, S. Liu, *Joule* **2018**, *2*, 1313.
[12] F. Sahli, J. Werner, B. A. Kamino, M. Brauninger, R. Monnard, B. Paviet-Salomon, L. Barraud, L. Ding, J. J. Diaz Leon, D. Sacchetto, G. Cattaneo, M. Despeisse, M. Boccard, S. Nicolay, Q. Jeangros, B. Niesen, C. Ballif, *Nat. Mater.* **2018**, *17*, 820.
[13] X. Zheng, B. Chen, J. Dai, Y. Fang, Y. Bai, Y. Lin, H. Wei, X. Zeng, J. Huang, *Nat. Energy* **2017**, *2*, 17102.
[14] Q. Jiang, L. Zhang, H. Wang, X. Yang, J. Meng, H. Liu, Z. Yin, J. Wu, X. Zhang, J. You, *Nat. Energy* **2017**, *2*, 16177.
[15] K. T. Cho, S. Paek, G. Grancini, C. Roldán-Carmona, P. Gao, Y. Lee, M. K. Nazeeruddin, *Energy Environ. Sci.* **2017**, *10*, 621.
[16] W. Rehman, D. P. McMeekin, J. B. Patel, R. L. Milot, M. B. Johnston, H. J. Snaith, L. M. Herz, *Energy Environ. Sci.* **2017**, *10*, 361.
[17] L. J. Richter, D. M. DeLongchamp, A. Amassian, *Chem. Rev.* **2017**, *117*, 6332.
[18] J. Schilipf, P. M. Buschbaum, *Adv. Energy Mater.* **2017**, *7*, 1700131.
[19] Q. Hu, L. Zhao, J. Wu, K. Gao, D. Luo, Y. Jiang, Z. Zhang, C. Zhu, E. Schaible, A. Hexemer, C. Wang, Y. Liu, W. Zhang, M. Gratzel, F. Liu, T. P. Russell, R. Zhu, Q. Gong, *Nat. Commun.* **2017**, *8*, 15688.
[20] K. Meng, L. Wu, Z. Liu, X. Wang, Q. Xu, Y. Hu, S. He, X. Li, T. Li, G. Chen, *Adv. Mater.* **2018**, *30*, 1706401.
[21] R. Munir, A. D. Sheikh, M. Abdelsamie, H. Hu, L. Yu, K. Zhao, T. Kim, O. E. Tall, R. Li, D. M. Smilgies, A. Amassian, *Adv. Mater.* **2017**, *29*, 1604113.
[22] T. Niu, J. Lu, R. Munir, J. Li, D. Barrit, X. Zhang, H. Hu, Z. Yang, A. Amassian, K. Zhao, S. Liu, *Adv. Mater.* **2018**, *30*, 1706576.
[23] S. Masi, A. Rizzo, R. Munir, A. Listorti, A. Giuri, C. Esposito, N. D. Treat, G. Gigli, A. Amassian, N. Stingelin, S. Colella, *Adv. Energy Mater.* **2017**, *7*, 1602600.
[24] X. Zhang, R. Munir, Z. Xu, Y. Liu, H. Tsai, W. Nie, J. Li, T. Niu, D. M. Smilgies, M. G. Kanatzidis, A. D. Mohite, K. Zhao, A. Amassian, S. Liu, *Adv. Mater.* **2018**, *30*, 1707166.
[25] X. Zhang, X. Ren, B. Liu, R. Munir, X. Zhu, D. Yang, J. Li, Y. Liu, D. Smilgies, R. Li, Z. Yang, T. Niu, X. Wang, A. Amassian, K. Zhao, S. Liu, *Energy Environ. Sci.* **2017**, *10*, 2095.
[26] Y. Zhang, P. Wang, M. Tang, D. Barrit, W. Ke, J. Liu, T. Luo, Y. Liu, T. Niu, D. Smilgies, Z. Yang, Z. Liu, S. Jin, M. G. Kanatzidis, A. Amassian, S. Liu, K. Zhao, *J. Am. Chem. Soc.* **2019**, *141*, 2684.
[27] N. Pellet, P. Gao, G. Gregori, T. Y. Yang, M. K. Nazeeruddin, J. Maier, M. Gratzel, *Angew. Chem., Int. Ed.* **2014**, *53*, 3151.
[28] G. E. Eperon, S. D. Stranks, C. Menelaou, M. B. Johnston, L. M. Herz, H. J. Snaith, *Energy Environ. Sci.* **2014**, *7*, 982.
[29] M. Alsari, O. Bikondoa, J. Bishop, M. Jalebi, L. Ozer, M. Hampton, P. Thompson, M. Horantner, S. Mahesh, C. Greenland, J. Macdonald, G. Palmisano, H. J. Sanith, D. G. Lidzey, S. D. Stranks, R. H. Friend, S. Lilliu, *Energy Environ. Sci.* **2018**, *11*, 383.
[30] D. P. McMeekin, G. Sadoughi, W. Rehman, G. E. Eperon, M. Saliba, M. T. Horantner, A. Haghighirad, N. Sakai, L. Korte, B. Rech, M. B. Johnston, L. M. Herz, H. J. Sanith, *Science* **2016**, *351*, 151.
[31] M. Abdi-Jalebi, Z. Andaji-Garmaroudi, S. Cacovich, C. Stavrakas, B. Philippe, J. M. Richter, M. Alsari, E. P. Booker, E. M. Hutter, A. J. Pearson, S. Lilliu, T. J. Savenije, H. Rensmo, G. Divitini, C. Ducati, R. H. Friend, S. D. Stranks, *Nature* **2018**, *555*, 497.
[32] L. Meng, J. You, T. F. Guo, Y. Yang, *Acc. Chem. Res.* **2016**, *49*, 155.
[33] H. S. Jung, N. G. Park, *Small* **2015**, *11*, 10.
[34] P. Gratia, I. Zimmermann, P. Schouwink, J. Yum, J. Audinot, K. Sivula, T. Wirtz, M. Nazeeruddin, *ACS Energy Lett.* **2017**, *2*, 2686.
[35] Z. Li, M. Yang, J.-S. Park, S.-H. Wei, J. J. Berry, K. Zhu, *Chem. Mater.* **2016**, *28*, 284.
[36] J. W. Lee, Z. Dai, C. Lee, H. M. Lee, T. H. Han, N. De Marco, O. Lin, C. S. Choi, B. Dunn, J. Koh, D. Di Carlo, J. H. Ko, H. D. Maynard, Y. Yang, *J. Am. Chem. Soc.* **2018**, *140*, 6317.
[37] A. Binek, F. C. Hanusch, P. Docampo, T. Bein, *J. Phys. Chem. Lett.* **2015**, *6*, 1249.
[38] C. C. Stoumpos, C. D. Malliakas, M. G. Kanatzidis, *Inorg. Chem.* **2013**, *52*, 9019.
[39] P. Gratia, I. Zimmermann, P. Schouwink, J. Yum, J. Audinot, K. Sivula, T. Wirtz, M. K. Nazeeruddin, *ACS Energy Lett.* **2017**, *2*, 2686.
[40] E. T. Hoke, D. J. Slotcavage, E. R. Dohner, A. R. Bowring, H. I. Karunadasa, M. D. McGehee, *Chem. Sci.* **2015**, *6*, 613.
[41] Y. H. Park, I. Jeong, S. Bae, H. J. Son, P. Lee, J. Lee, C.-H. Lee, M. J. Ko, *Adv. Funct. Mater.* **2017**, *27*, 1605988.
[42] C. Yi, J. Luo, S. Meloni, A. Boziki, N. Astani, C. Gratzel, S. Zakeeruddin, U. Rothlisberger, M. Gratzel, *Energy Environ. Sci.* **2016**, *9*, 656.
[43] J. Lee, S. Baik, *RSC Adv.* **2018**, *8*, 1005.
[44] A. Sharenko, C. Mackeen, L. Jewell, F. Bridges, M. Toney, *Chem. Mater.* **2017**, *29*, 1315.
[45] J. C. Hamill, J. Schwartz, Y. Loo, *ACS Energy Lett.* **2018**, *3*, 92.
[46] D. Barrit, P. Cheng, M. Tang, K. Wang, H. Dang, D. Smilgies, S. Liu, T. Anthopoulos, K. Zhao, A. Amassian, *Adv. Funct. Mater.* **2019**, https://doi.org/10.1002/adfm.201807544.
[47] M. Tang, D. Barrit, R. Munir, R. Li, J. Barbe, D. Smilgies, S. Gobbo, T. Anthopoulos, A. Amassian, *Sol. RRL* **2019**, https://doi.org/10.1002/solr.201800305.
[48] H. X. Dang, K. Wang, M. Ghasemi, M.-C. Tang, M. De Bastiani, E. Aydin, E. Dauzon, D. Barrit, J. Peng, D.-M. Smilgies, S. De Wolf, *A. Amassian. Joule* **2019**, https://doi.org/10.1016/j.joule.2019.05.016.
[49] D. Kubick, D. Prochowicz, A. Hofstetter, S. Zakeeruddin, M. Gratzel, L. Emsley, *J. Am. Chem. Soc.* **2017**, *139*, 14713.
[50] M. Jalebi, Z. Garmaroudi, A. Pearson, G. Divitini, S. Cacovich, B. Philippe, H. Rensmo, C. Ducati, R. H. Frient, S. D. Stranks, *ACS Energy Lett.* **2018**, *3*, 2671.
[51] M. Saliba, T. Matsui, K. Domanski, J. Seo, A. Ummadisingu, S. Zakeeruddin, J. Correa-Baena, W. R. Tress, A. Abate, A. Hagfeldt, M. Gratzel, *Science* **2016**, *354*, 206.
[52] K. Wang, M. Neophytou, E. Aydin, M. Wang, T. Laurent, G. Harrison, J. Liu, W. Liu, M. Bastiani, J. Khan, T. Anthopoulos, F. Laquai, S. Wolf, *Adv. Mater. Interfaces* **2019**, *10*, 1900434.
[53] H. Tan, A. Jain, L. Voznyy, X. Lan, F. Arquer, J. Fan, R. Bermudez, M. Yuan, B. Zhang, Y. Zhao, F. Fan, P. Li, L. Quan, Y. Zhao, Z. Lu, Z. Yang, S. Hoogland, E. H. Sargent, *Science* **2017**, *355*, 722.

© 2019 WILEY-VCH Verlag GmbH & Co. KGaA, Weinheim